Can the Nucleation Phase be Generated on a Sub-fault Linked to the Main Fault of an Earthquake?

Jeen-Hwa Wang[1,2]

[1] Institute of Earth Sciences, Academia Sinica, Taipei, TAIWAN
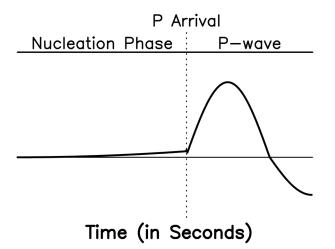[2] Department of Earth Sciences, National Central University, Taoyuan, Taiwan
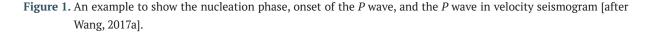
Abstract

We study the effects of seismic coupling, friction, viscosity, and inertia on earthquake nucleation based on a two-body spring-slider model in the presence of thermal-pressurized slip-dependent friction and viscosity. Seismic coupling of the system is represented by the stiffness ratio $s = K/L$ where K is the coil spring between two sliders and L is the leaf spring between a slider and the background plate. Weak seismic coupling with $s < 1$ is used in this study. The masses of the two sliders are m_1 and m_2, respectively. The frictional and viscous effects at slider i (i = 1, 2) are specified by the static friction force, f_{oi}, the characteristic displacement, U_{ci}, and viscosity coefficient, η_v, respectively. Numerical simulations show that the s is not a major factor in generating the nucleation phase. Friction and viscosity can both lengthen the natural period of the system and viscosity increases the duration time of motion of the slider. Higher viscosity causes lower particle velocities than lower viscosity. Simulation results exhibit that the ratios $\gamma = \eta_2/\eta_1$, $\phi = f_{o2}/f_{o1}$, $\psi = U_{c2}/U_{c1}$, and $\mu = m_2/m_1$ are four factors in influencing the generation of nucleation phase at slider 1 and the formation of P wave of an event at slider 2. That simulated waveforms with $\gamma > 1$, $1.15 > \phi > 1$, $\psi < 1$, and $\mu < 30$ are consistent with the observations suggests the possibility of generation of nucleation phase on a sub-fault. Results also exhibit independence of P wave at slider 2 on the shape and duration time of nucleation phase at slider 1.

Keywords: Nucleation phase; Two-body spring-slider model; Stiffness ratio; Thermal-pressurized slip-dependent friction; Viscosity; Inertial effect

1. Introduction

The presence of nucleation phase before the P waves (see Figure 1) was suggested by early theoretical studies [e.g., Andrews, 1976; Brune, 1979; Dieterich, 1986, 1992; Das and Scholz, 1981] and laboratory experiments [Dieterich, 1979; Ohnaka et al., 1987]. Some studies [e.g., Scholz et al., 1972; Dieterich, 1981; Ohnaka and Yamashita, 1989; Ohnaka, 1992; Ohnaka and Kuwahara, 1990; Kato et al., 1994; Roy and Marone, 1996; Lu et al., 2010; Latour et al., 2013; Kaneko et al., 2016] also indicated that the nucleation process behaves like a transition from quasi-static slip (without the inertial effect) to (unstable) dynamic motion (with the inertial effect) when the slip speeds become high enough to make the inertial effect dominate frictional resistance under some conditions. The study of nucleation

Figure 1. An example to show the nucleation phase, onset of the *P* wave, and the *P* wave in velocity seismogram [after Wang, 2017a].

phase is not only a basic problem of earthquake physics but also an important one for early warming, prediction, and hazard assessment of earthquakes.

Umeda [1990] first recognized the existence of nucleation phase in velocity seismograms. Since then, numerous seismologists have also observed the nucleation phases [e.g., Iio, 1992, 1995; Ellsworth and Beroza, 1995; Beroza and Ellsworth, 1996; Mori and Kanamori, 1996; Ruiz et al., 2017]. There was a debate concerning the correlation between the duration time, T_D, of nucleation phase and the magnitude, M, of the earthquake occurring immediately after the nucleation phase. Ellsworth and Beroza [1995] and Beroza and Ellsworth [1996] assumed a positive correlation of T_D to M. Whereas, Mori and Kanamori [1996] observed independence of the *P* waves on the shape of nucleation phase in a large magnitude range. Ellsworth and Beroza [1998] confirmed the results observed by Mori and Kanamori [1996].

Friction and viscosity are two major factors in controlling the complicated earthquake rupture processes including nucleation [Wang, 2016; and cited references therein]. Analytic solutions and numerical simulations for exploring the nucleation phase have been made based on the infinite dislocation models, crack models, and spring-slider models by using different friction laws [Beeler, 2004; Bizzarri, 2009, 2011a,b; Tal et al., 2018; Wang, 2016, 2017a; and cited references therein]. Iio [1992, 1995] stressed that the nucleation phase cannot be interpreted by any theoretical source model with a constant kinematic friction and a constant rupture velocity. Mori and Kanamori [1996] claimed that any model having a similar initial rupture can describe the nucleation phases of earthquakes of all sizes, and thus it is difficult to estimate the magnitude of an earthquake just from its nucleation phase. They also stressed that curvature seen in the nucleation phases is caused by an-elasticity.

Since the present study concentrates on the generation of nucleation phase on a sub-fault and initiation of dynamic slip (or an earthquake) on a main fault, a two-body spring-slider (SS) model, which has been used to approach an earthquake fault by numerous authors [e.g., Galvanetto, 2002; Turcotte, 1992; Wang, 2007, 2017b, 2020], by considering the two sliders as two fault segments, is taken into account. Although the two-body SS model is simplified from the many-body SS model [Burridge and Knopoff, 1967], it can still provide significant information about the properties of real earthquakes [Turcotte, 1992]. Of course, a many-body SS model can provide more information than a two-body SS one. Nevertheless, it is easier to explore the generation of nucleation phase on a sub-fault and main dynamic slip on the main fault by using a two-body SS model than by using a many-body one. Note that the many-body SS model and its simplified and modified models are actually a discretization of a continuous fault and thus an approximation of a problem of continuum mechanics.

Some of previous theoretical studies concerning the nucleation phase based on the SS model and its modified and simplified forms are briefly described here. Brantut et al. [2011] concluded that metamorphic dehydration influences the nucleation of unstable slip and could be an origin for slow-slip events in subduction zones. Ueda et al. [2014, 2015] and Kawamura et al. [2018] pointed out that the nucleation process includes the quasi-static initial phase, the unstable acceleration phase, and the high-speed rupture phase (i.e., a mainshock) and recognized two kinds of nucleation lengths, i.e., L_{sc} and L_c which are affected by model parameters, yet not by the earthquake size. The L_{sc} related to the initial phase exists only for a weak frictional instability regime; while the L_c associated with the

acceleration phase exist for both weak and strong instability regimes. They also found that in the initial phase up to L_{sc}, the sliding velocity is an order of magnitude of the plate speed; while at a certain stage of the acceleration phase it becomes higher and thus can be observed.

On the other hand, numerous lower-degrees-of-freedom models that have the geometric structure consisting of few, large patches have also been assumed by numerous authors [e.g., Ruff, 1992; Turcotte, 1992; Rice, 1993] to investigate fault dynamics. Interaction between different fault patches may play a key role on the dynamics of earthquake ruptures. The failure of a fault segment triggered by slip of another fault segment has been long and widely studied. The discrete fault model consisting of two segments having different mechanical properties may exhibit a very rich dynamics and make it possible to study in detail fault evolution during both coseismic slip and interseismic intervals. Some examples are given below. Viscoelasticity was taken into account by Dragoni and Lorenzano [2015]. Fault evolution during interseismic intervals was considered by Dragoni and Piombo [2015] and Lorenzano and Dragoni [2018]. The velocity dependent term was introduced by Dragoni and Santini [2015] and its role was further examined by Dragoni and Santini [2017] and Dragoni and Tallarico [2016]. The presence of different mechanical properties, including different masses that would lead to the inertial effect, on two fault segments was considered by Dragoni and Lorenzano [2017].

Although the frictional effect on earthquake nucleation has been long and widely studied as mentioned above, the studies of viscous effect on earthquake ruptures are rare. The viscous effect mentioned in Rice et al. [2001] is actually an implicit factor which is included within the direct effect of rate- and state-dependent friction law. Wang [2017a] took viscosity into account for studying the nucleation phase by assuming a temporal change of high viscosity to low viscosity during an earthquake rupture based on a one-body SS model with thermal-pressurized slip-weakening friction. His results show a temporal variation from nucleation phases to P wave and the amplitude of P wave, which is associated with the earthquake magnitude, does not depend on the duration time of the former.

As mentioned above, the nucleation process behaves like a transition from quasi-static slip (without the inertial effect) to (unstable) dynamic motion (with the inertial effect) when the slip speeds become high enough to make the inertial effect dominate frictional resistance under some conditions. This assumes that the inertial effect must be taken into account.

In most of previous studies, both the nucleation phase and the P wave are assumed to occur on the same fault. There is an interesting question: Can the nucleation phase happen on a sub-fault which links to the main fault of an earthquake? In order to answer this question, in this work I will explore the frictional, viscous, and inertial effects on the generation of nucleation phase on a fault and then the transition from it to the P wave on the other based on a two-body SS model. The friction force caused by thermal pressurization is slip-weakening and the viscosity is represented by an explicit parameter. The study of inertial effect on nucleation phase is rare. This effect is implicitly included in the thermal-pressurized friction used by Brantut et al. [2011]. Wang [2020] addressed the importance of inertial effect on the earthquake nucleation. In this study, the inertial effect will also be taken into account.

2. Two-body spring-slider model

The two-body SS model (Figure 2) consists of two sliders of mass m_i (i = 1, 2) and three springs. A detailed description of the model can be seen in Wang [2017b] and only a brief explanation is given here. The equation of motion of the system is

$$m_1 d^2 u_1 / dt^2 = K(u_2 - u_1) - L_1(u_1 - v_P t) - F_1(u_1) - \Phi(v_1) \tag{1a}$$

$$m_2 d^2 u_2 / dt^2 = K(u_1 - u_2) - L_2(u_2 - v_P t) - F_2(u_2) - \Phi(v_2). \tag{1b}$$

The u_i (i = 1, 2) is the displacement of the i-th slider measured from its initial equilibrium position along the x-axis. The K is the strength of the coil spring between two sliders and the L_i (i = 1, 2) is the strength of the leaf spring to yield the driving force on the i-th slider from a moving plate with a constant speed v_P. Considering the two sliders to represent two segments of an earthquake fault, the coupling between the moving plate and
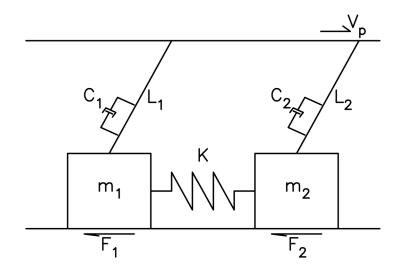
Figure 2. A two-body spring-slider model: F_i = the friction force at the i-th slider, m_i = the mass of the i-th slider, K = the stiffness between two sliders, L_i = the stiffness between the i-th slider and the moving plate, C_i = the viscosity coefficient between the i-th slider and the moving plate, and v_p = the velocity of the moving plate, and u_i (i = 1, 2) is the displacement of the i-th slider [after Wang, 2017b].

each slider could be equal, thus giving $L_1 = L_2 = L$. $F_i(u_i)$ (i = 1, 2) is the frictional force on the i-th slider. Wang [2013] took $F(u) = F_o exp(-u/u_c)$, where F_o and u_c are, respectively, the static friction force and characteristic slip displacement, to study earthquake dynamics. This friction force is slip-weakening and caused by the adiabatic-undrained-deformation (AUD)-type thermal pressurization [Rice, 2006].

The friction law due to thermal pressurization must refer to the solution of uniform slip made by Lachenbruch [1980]. This friction law is essentially independent of the slip velocity and only implicitly depends on velocity through the seismic slip. Within the normal 1-mm thick shear zone, most of the shearing seems to occur in a shear localized zone having a thickness of 100-300 μm. Such thicknesses are smaller than those of hydraulic and thermal boundary layers that have developed near faults during significant earthquakes [e.g., Rice, 2006]. Hence, Mase and Smith [1987] and Lee and Delaney [1987] assumed that it is more appropriate to consider the occurrence of slip in a zone of zero thickness, i.e., a mathematical plane. On such a plane, the Lachenbruch solution is unstable [see Rice 2006] and for large values of the seismic slip displacement, strain will localize on a mathematical plane of zero thickness [see Mase and Smith 1987].

Two reasons to explain why slip-dependent friction is taken in this study are: (1) Madariaga and Cochard [1994] pointed out that purely velocity-dependent friction could yield unphysical phenomena and mathematically ill-posed problems and Ohnaka [2003] also stressed that the pure rate-dependent friction law is not a one-valued function of velocity. (2) The above-mentioned slip-dependent friction law comes from the end-member model, i.e., the adiabatic, undrained deformation (AUD) model, of the thermal pressurization model in the fault zone proposed by Rice [2006]. The other end-member model is the slip on a plane (SOP) model. For the AUD model, the sliding slip is dependent upon the varying sliding velocity; while for the SOP model, the sliding velocity is always constant in the course of rupture processes. In the present study, since I used the AUD model, slip-dependent friction is intrinsically dependent on velocity. An example of the variations of $F(u)$ versus u for F_o = 1 N and u_c = 0.1, 0.3, 0.5, 0.7, and 0.9 m is displayed in Figure 3 in which $F(u)$ decreases with increasing u, and the decreases rate is higher for smaller u_c than for larger u_c. This indicates that the force drop decreases with increasing u_c for the same final slip.

The function $\Phi(v_i)$, where $v_i = du_i/dt$ is the particle velocity, denotes a velocity-dependent viscous force, which is represented by a dash-pot in Figure 2, due to the existence of viscosity in the fault zone. A detailed description about the mechanism of viscous force can be seen in Wang [2017a,b]. According to Stokes' law, Wang [2016] suggested the viscous force to be $\Phi = Cv$, where $C = 6\pi R\upsilon$ (with a unit of N(m/s)$^{-1}$) is the damping coefficient of a sphere of radius R in a fluid of viscosity υ [see Kittel et al. 1968]. The two sliders rest in an equilibrium state at time $t = 0$. Note that this model addresses only the strike-slip component and thus cannot completely represent earthquake ruptures, which also consist of transpressive components. Nevertheless, simulation results of this model can still provide significant information on earthquake ruptures.
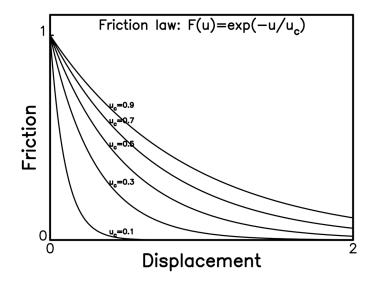
Figure 3. The variations of friction force with sliding displacement for $u_c = 0.1, 0.3, 0.5, 0.7,$ and 0.9 m when $F_o = 1$ force unit [after Wang, 2017b].

Substituting the friction and viscous laws into Equation (1) leads to

$$m_1 d^2 u_1/dt^2 = K(u_2 - u_1) - L(u_1 - v_{Pt}) - F_{o1} exp(-u_2/u_{c1}) - C_1 du_1/dt \tag{2a}$$

$$m_2 d^2 u_2/dt^2 = K(u_1 - u_2) - L(u_2 - v_{Pt}) - F_{o2} exp(-u_2/u_{c2}) - C_2 du_2/dt \tag{2b}$$

To deal with the problem easily, it is usual to normalize Equation (2) based on the normalization parameters. Wang [1995] defined the stiffness ratio, s, to be the ratio of K to L, i.e., $s = K/L$. Wang [2017b] defined the normalization parameters for Equation (2). However, in his study he took $m_1 = m_2$, and thus he did not consider the cases with $m_1 \neq m_2$. While, in this study m_2 could be larger than m_1, thus leading to the inertial effect. Hence, the parameters normalizing Equation (2) are: $m_1 = m$, $m_2 = \mu m$, $F_{o1} = F_o$, $F_{o2} = \phi F_o$, $D_o = F_o/L$, $\omega_{o1} = \omega_o = (L/m)^{1/2}$, $\omega_{o2} = \mu^{-1/2}\omega_o$, $\tau = \omega_o t, u_{c1} = u_c, u_{c2} = \psi u_c, U_{c1} = u_c/D_o, U_{c2} = \psi u_c/D_o, f_{o1} = f_o = F_o/D_o, f_{o2} = \phi f_o, \eta_1 = C_1\omega_o/L, \eta_2 = C_2\mu^{-1/2}\omega_o/L, \gamma = \eta_2/\eta_1,$ and $V_P = v_P/D_o\omega_o$. Defining $U_i = u_i/D_o$ and $V_i = dUi/d\tau$ leads to $du_i/dt = [F_o/(mL)^{1/2}]dU_i/d\tau$ and $d^2u_i/dt^2 = (F_o/m)d^2U_i/d\tau^2$. Inserting these normalization parameters with $f_o = 1$ into Equation (2) results in the following equations:

$$d^2 U_1/d_\tau^2 = s(U_2 - U_1) - (U_1 - V_P\tau) - exp(-U_1/U_{c1}) - \eta_1 dU_1/d\tau \tag{3a}$$

$$d^2 U_2/d_\tau^2 = [s(U_1 - U_2) - (U_2 - V_P\tau) - \phi exp(-U_2/U_{c2}) - \eta_2 dU_2/d\tau]/\mu. \tag{3b}$$

Let $y_1 = U_1$, $y_2 = U_2$, $y_3 = dU_1/d\tau$, and $y_4 = dU_2/d\tau$ and then re-write Equation (3) to be four first-order differential equations:

$$dy_1/d\tau = y_3 \tag{4a}$$

$$dy_2/d\tau = y_4 \tag{4b}$$

$$dy_3/d\tau = -(s+1)y_1 + sy_2 - exp(-y_1/U_{c1}) - \eta_1 y_3 + V_P\tau \tag{4c}$$

$$dy_4/d\tau = [sy_1 - (s+1)y_2 - \phi exp(-y_2/\psi U_{c1}) - \gamma\eta_1 y_4 + V_P\tau]/\mu. \tag{4d}$$

Since it is difficult to analytically solve Equation (4), only numerical simulations using the fourth-order Runge-Kutta method [see Press et al., 1986] are performed in this study. Note that the sliders are restricted to move only along the positive direction, that is, $Vi \geq 0$ and $Ui \geq 0$ (i = 1, 2).

3. Numerical simulations

Before performing numerical simulations, it is necessary to consider the acceptable values of model parameters. Strong seismic coupling can make the two sliders move almost simultaneously. In order to allow independent motion for each slider, the value of s should be small. Numerical tests [e.g., Wang, 2017b] show weak coupling as $s < 5$ and strong coupling as $s \geq 5$ for a two-body spring-slider system. Hence, $s < 5$ is considered in this study. In general, v_P is $\sim 10^{-9}$ m/s and thus V_P is $\sim 10^{-9}$ when $D_o\omega_o$ is an order of magnitude of 1 m/sec. Simulation results could be
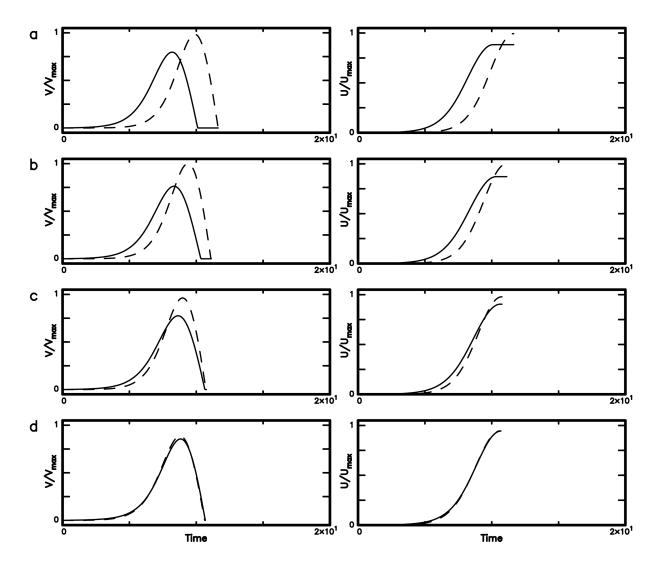

Figure 4. The time sequences of V/V_{max} ($V_{max} = 0.456$) and U/U_{max} ($U_{max} = 1.355$): (a) for $s = 0.06$, (b) for $s = 0.12$, (c) for $s = 0.30$, and (d) for $s = 0.48$ when $\mu = 1$, $f_{o1} = 1.0$ and $f_{o2} = 1.0$ (with $\phi = 1$), $U_{c1} = 0.5$ and $U_{c2} = 0.5$ (with $\psi = 1$), and $\eta_1 = 0$ and $\eta_2 = 0$ (with $\gamma = 1$).

influenced by using various time steps, $\delta\tau$. Practical tests suggest that simulation results show numerical stability when $\delta\tau < 0.05$. The time step is taken to be $\delta\tau = 0.02$ hereafter. When $V_P\tau = exp(-y_1/U_{c1})$ on slider 1 from Equation (4c), the force exerted from the moving plate is just equal to f_{oi}. Although in principle slider 1 can start to move under this condition, in practice the computation cannot go ahead because all values are zero. An initial force, δf, is necessary to kick off slider 1. Note that the value of δf can affect the computational results [Carlson et al., 1991]. A very small value of δf cannot enforce slider 1 to move; while a large one will dominate the whole computation process. Numerical tests show that $\delta f = 10^{-3}$ is appropriate for numerical simulations.

Numerical simulations are made under various values of model parameters for showing the effects caused by seismic coupling, friction, viscosity, and inertial effect. Simulation results are displayed in Figures 4-10 which include the time variations in V/V_{max} (in the left-hand-side panels) and U/U_{max} (in the right-hand-side panels). The values of V_{max} and U_{max} are given below. In Figures 4-10, the simulation results at slider 1 and slider 2 are represented, respectively, by a solid line and a dotted one.

It is necessary to examine the lower-bound value of s for yielding strong enough seismic coupling between the two sliders. Numerical tests exhibit that slider 2 cannot move for $s < 0.06$ when other model parameters are equal at the two sliders. Hence, $s = 0.06$ is almost the lower bound of seismic coupling for most of simulations. On the other hand, numerical tests suggest that when $s > 0.48$, the solid and dashed lines coincide. This means that large s having strong seismic coupling leads to almost simultaneous motions of the two sliders. The results for the effect due to seismic coupling are displayed in Figure 4 where the values of s are: (a) for $s = 0.06$, (b) for $s = 0.12$, (c) for $s = 0.30$,
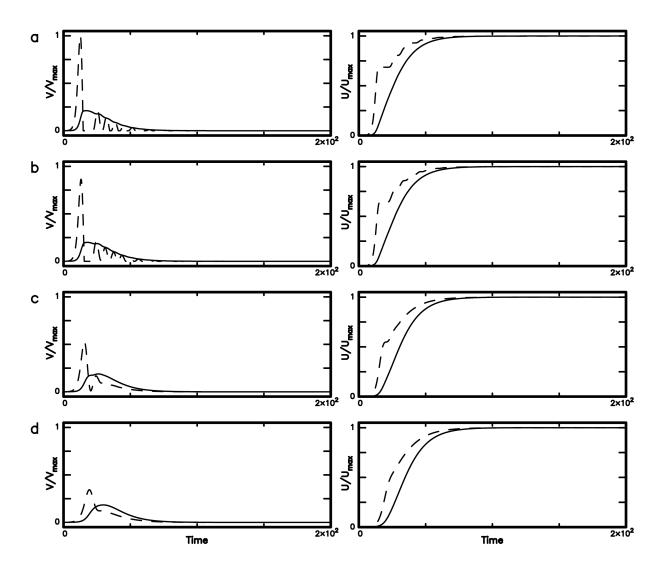

Figure 5. The time sequences of V/V_{max} ($V_{max} = 0.142$) and U/U_{max} ($U_{max} = 0.798$): (a) for $\gamma = 0.00$, (b) for $\gamma = 0.01$, (c) for $\gamma = 0.05$, and (d) for $\gamma = 0.10$ (from weak viscosity ratio to strong viscosity ratio) when $s = 0.48$, $\mu = 1$, $\eta_1 = 10$, $f_{o1} = 1.0$ and $f_{o2} = 1.0$ (with $\phi = 1$), and $U_{c1} = 0.5$ and $U_{c2} = 0.5$ (with $\psi = 1$).

and (d) for $s = 0.48$ (i.e., from very weak coupling to weak coupling) when $f_{o1} = f_{o2} = 1.0$ (with $\phi = 1$), $U_{c1} = U_{c2} = 0.5$ (with $\psi = 1$), and $\eta_1 = \eta_2 = 0$ (with $\gamma = 1$). The value of s is 0.48 in Figures 5-7 and Figure 9 to explore which factor can separate the motions of the two sliders.

Figures 5-8 display the results due to different values of viscosity at the two sliders when other parameter are fixed: (a) for $\gamma = 0.00$ (or $\eta_2 = 0$), (b) for $\gamma = 0.01$ (or $\eta_2 = 0.1$), (c) for $\gamma = 0.05$ (or $\eta_2 = 0.5$), and (d) for $\gamma = 0.10$ (or $\eta_2 = 1$) (i.e., from weak viscosity ratio to strong viscosity ratio) when $\eta_1 = 10$. In Figure 5, the values of other model parameters are $\mu = 1$, $\eta_1 = 10$, $s = 0.48$, $f_{o1} = f_{o2} = 1.0$ (with $\phi = 1$), and $U_{c1} = U_{c2} = 0.5$ (with $\psi = 1$). The figure displays the presence of the P wave at slider 2. Numerical tests reveal that the P wave at slider 2 cannot be generated especially for $\gamma \geq 0.05$ when $\eta_1 > 70$, and the solutions are just like Figure 4 when $\eta_1 < 5$. Hence, η_1 is taken to be 10 in Figures 6-10. The effect due to different static friction strengths at the two sliders is displayed in Figure 6 with $\mu = 1$, $\eta_1 = 10$, $s = 0.48$, $f_{o1} = 1.0$ and $f_{o2} = 1.1$ (with $\phi = 1.1$), and $U_{c1} = U_{c2} = 0.5$ (with $\psi = 1$). The figure exhibits the presence of a nucleation phase at slider 1. Numerical tests exhibit that when $\phi > 1.15$, the P wave at slider 2 cannot be generated. Hence, ϕ is taken to be 1.1 in Figures 7-10. The effect due to different characteristic displacements at the two sliders is displayed in Figure 7 with $\mu = 1$, $\eta_1 = 10$, $s = 0.48$, $f_{o1} = 1.0$ and $f_{o2} = 1.1$ (with $\phi = 1.1$), and $U_{c1} = 0.5$ and $U_{c2} = 0.1$ (with $\psi = 0.2$).

The figure shows the presence of a nucleation phase at slider 1. Numerical tests exhibit that when $U_{c1} > 0.5$, the P wave at slider 2 cannot be generated. Hence, U_{c1} is taken to be 0.5 in Figures 8-10. In order to consider weaker seismic coupling on the simulated waveforms, smaller s is taken into account. Numerical tests exhibit that when
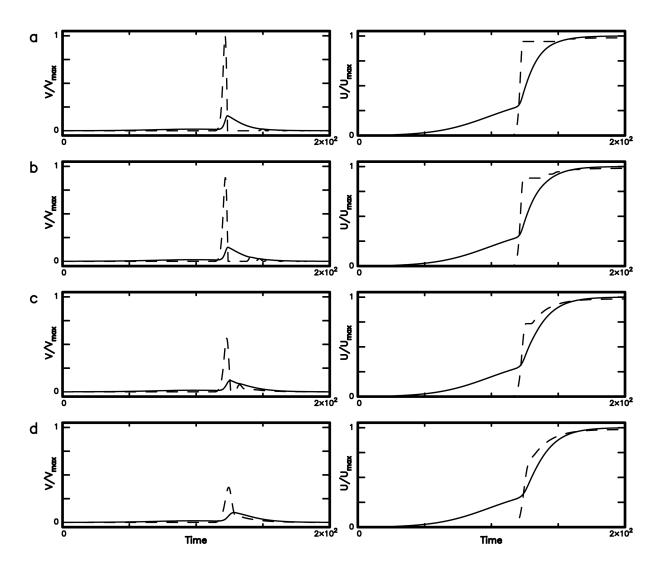

Figure 6. The time sequences of V/V_{max} ($V_{max} = 0.226$) and U/U_{max} ($U_{max} = 0.766$): (a) for $\gamma = 0.00$, (b) for $\gamma = 0.01$, (c) for $\gamma = 0.05$, and (d) for $\gamma = 0.10$ (from weak viscosity ratio to strong viscosity ratio) when $s = 0.48$, $\mu = 1$, $\eta_1 = 10$, $f_{o1} = 1.0$ and $f_{o2} = 1.1$ (with $\phi = 1.1$), and $U_{c1} = 0.5$ and $U_{c2} = 0.5$ (with $\psi = 1$).

$s < 0.17$, the P wave at slider 2 cannot be generated. Hence, s is also taken to be 0.17 in Figure 8 with $\mu = 1$, $\eta_1 = 10$, $s = 0.17$, $f_{o1} = 1.0$ and $f_{o2} = 1.1$ (with $\phi = 1.1$), and $U_{c1} = 0.5$ and $U_{c2} = 0.1$ (with $\psi = 0.2$).

Figures 9 and 10 display the results for the inertial effect due to different masses of the two sliders: (a) for $\mu = 1$, (b) for $\mu = 5$, (c) for $\mu = 10$, and (d) for $\mu = 30$ (i.e., from weak mass ratio to strong mass ratio) when $\eta_1 = 10$, $f_{o1} = 1.0$ and $f_{o2} = 1.1$ (with $\phi = 1.1$), $U_{c1} = 0.5$ and $U_{c2} = \gamma.1$ (with $\psi = 0.2$), and $\eta_1 = 10$ and $\eta_2 = 0$ (with $\gamma = 0$). The main difference between the two figures is the use of different values of seismic coupling: $s = 0.48$ in Figure 9 and $s = 0.17$ in Figure 10.

Numerical results show that the maximum values of velocities (V_{max}) and displacements (U_{max}) are: 0.456 and 1.355, respectively, in Figure 4; 0.142 and 0.798, respectively, in Figure 5; 0.226 and 0.766, respectively, in Figure 6; 0.781 and 1.403, respectively, in Figure 7; 0.903 and 1.778, respectively, in Figure 8; 0.781 and 1.505, respectively, in Figure 9; and 0.903 and 1.790, respectively, in Figure 10. In order to conveniently compare simulated results displayed in the panels of a figure, the time variations in velocity and displacement have been normalized, respectively, by related values of V_{max} and U_{max}.

4. Discussion

4.1 Seismic coupling effect

Figure 4 shows the results when $s = 0.06$, 0.12, 0.30, and 0.48 (upside down). In the left-hand-side panels, V/V_{max} increases from a small value to the peak and then decreases again to a small one. The dashed line separates from the solid line for small s, while the two lines almost coincide for large s, thus indicating an increase in the degree of coupling between the two sliders with s. Meanwhile, the peak velocity appears earlier and is higher at slider 1 than at slider 2, thus exhibiting the presence of directivity effect because the system moves from slider 1 to slider 2. However, this figure does not exhibit the existence of long-period nucleation phase. Hence, seismic coupling is not a significant factor in generating nucleation phase. In the right-hand-side panels, U/U_{max} increases from a small value to the final slip. The above-mentioned phenomena about the two curves for V/V_{max} can also be seen for U/U_{max}. In addition, a small differences in final displacements between the two sliders decrease with increasing s.

4.2 Viscous effect

Based on a one-body SS model, Wang [2017a] addressed that a change of viscosity from a larger value to a small one in two time stages during slippage yields the nucleation phase and the P wave, respectively, in the first and second stages. Hence, simulations are made by setting $\eta_1 = 10$ and letting $\eta_2 = 0$, 0.1, 0.5, and 1 or $\gamma = 0.00$, 0.01, 0.05, 0.10 (i.e., from weak viscosity ratio to strong viscosity ratio) when $s = 0.48$, $f_{o1} = f_{o2} = 1.0$ (with $\phi = 1$), $U_{c1} = U_{c2} = 0.5$ (with $\psi = 1$), and $\eta_1 = \eta_2 = 0$ (with $\gamma = 1$). Results are shown in Figure 5. In the left-hand-side panels, V/V_{max} at slider 1 increases from a small value to a peak and then decreases again to a small one; while V/V_{max} at slider 2 increases rapidly from a small one to a peak, then oscillates and decreases again to a small one. The degree of oscillations at slider 2 decreases with increasing γ. The dashed line separates from the solid line for the four values of γ, thus indicating the viscous effect on the velocity waveforms. That the peak velocity is higher at slider 2 than at slider 1 shows the directivity effect from left to right. The peak velocity at slider 2 decreases with increasing γ, yet not at slider 1. Although slider 1 started to move earlier than slider 2, the peak velocity comes later at it than at sider 2. The occurrence time of the peak velocity of slider 2 slightly increases with γ. The panels exhibit a short-time nucleation phase plus a smaller event at slider 1 and a larger event with a stronger P wave at slider 2. Hence, there are two sub-events during the whole rupture process. The appearance of oscillations behind the first peak velocity at slider 2 indicates the existence of few smaller-sized sub-events with lower peak velocities after the main one. The number of such sub-events decreases with increasing γ.

In the right-hand-side panels of Figure 5, U/U_{max} first increases more rapidly at slider 2 (displayed by a dashed line) than at slider 1 (shown by a solid line) and finally two lines merge together, thus exhibiting the same final displacement at the two sliders. It is clear that the dashed line is less smooth than the solid line because of a few oscillations representing smaller-sized sub-events at slider 2. Of course, the degree of smoothness increases with γ. This is due to a decrease in the number of sub-events with increasing γ.

Although there is a long-period waveform at slider 1 in Figure 5, its peak velocity comes after that of a short-period P wave at slider 2. This does not exhibit transition from quasi-static motions to dynamic ruptures as shown from observations, and thus the whole waveform at slider 1 cannot be classified to be the nucleation phase. Hence, different viscosity coefficients between the two sliders are not the unique factor in yielding the nucleation phase, and thus the differences in other model parameters must also be taken into account.

4.3 Frictional effect

The frictional effect includes two components: the static friction force represented by the frictional strength (i.e., f_{o1} and f_{o2} at slider 1 and slider 2, respectively) and the characteristic displacements of friction law (i.e., U_{c1} and U_{c2} at slider 1 and slider 2, respectively). The results will be explained in three parts below.

First, we consider different values of s, f_{o1}, and f_{o2}. Figure 6 exhibits the results for $f_{o1} = 1.0$ and $f_{o2} = 1.1$ (with $\phi = 1.1$) when $s = 0.48$, $U_{c1} = U_{c2} = 0.5$ (with $\psi = 1$), $\eta_1 = 10$, and $\gamma = 0.00$, 0.01, 0.05, and 0.10. The left-hand-side panels show the presence of a very long-duration nucleation phase in the front of a strong P wave of an event at slider 2 and a small event at slider 1. This phenomenon is named as the NP-PW pattern hereafter. The duration time of nucleation phase at slider 1 slightly increases with the peak velocity at slider 2. Although slider 1 started to move earlier than slider 2, the peak velocity at the former comes later than that at the latter. Unlike Figure 5, the
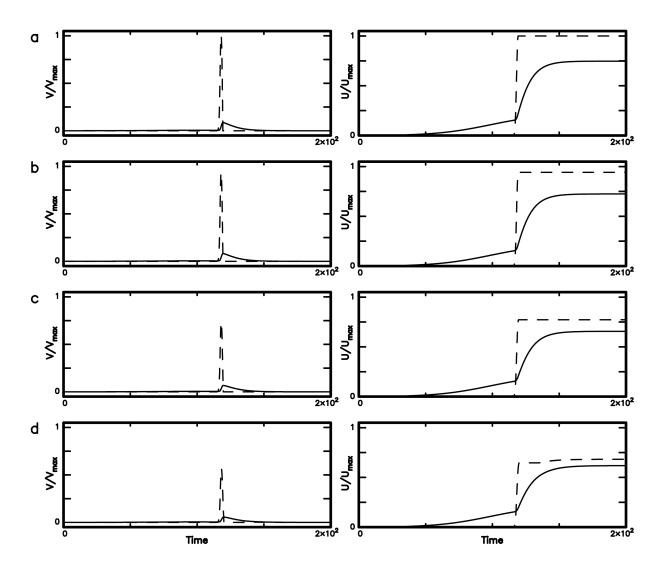

Figure 7. The time sequences of V/V_{max} ($V_{max} = 0.781$) and U/U_{max} ($U_{max} = 1.403$): (a) for $\gamma = 0.00$, (b) for $\gamma = 0.01$, (c) for $\gamma = 0.05$, and (d) for $\gamma = 0.10$ (from weak viscosity ratio to strong viscosity ratio) when $s = 0.48$, $\mu = 1$, $\eta_1 = 10$, $f_{o1} = 1.0$ and $f_{o2} = 1.1$ (with $\phi = 1.1$), and $U_{c1} = 0.5$ and $U_{c2} = 0.1$ (with $\psi = 0.2$).

occurrence time of the peak velocity at slider 2 slightly decreases with increasing γ. This might be caused by $f_{o1} < f_{o2}$. Although a small bump appears in the waveform of slider 1, its peak velocity is much smaller than that of slider 2. The difference in the peak velocities between the two sliders decreases with increasing γ. Hence, unlike Figure 5 there is almost only one event in the whole rupture process in Figure 6. After slider 2 stopped, slider 1 still moves. Meanwhile, the maximum peak velocity is higher in Figure 6 than in Figure 5. The right-hand-side panels of Figure 6 show that U/U_{max} at both slider 1 (displayed by a solid line) and slider 2 (displayed by a dashed line) increases with time. A small event at slider 1 and a large one at slider 2 appear almost simultaneously. Unlike Figure 5, U/U_{max} at slider 2 suddenly jumps from a small value to the final slip.

Secondly, we consider $U_{c1} \neq U_{c2}$. Figure 7 exhibits the results for $U_{c1} = 0.5$ and $U_{c2} = 0.1$ (with $\psi = 0.2$) when $s = 0.48$, $f_{o1} = 1.0$ and $f_{o2} = 1.1$ (with $\phi = 1.1$), $\eta_1 = 10$, and $\gamma = 0.00, 0.01, 0.05$, and 0.10. The left-hand-side panels of Figure 7 show the NP-PW pattern. The duration time of nucleation phase at slider 1 only slightly increases with the peak velocity at slider 2. After slider 2 stopped, slider 1 still moves and its peak velocity comes after that of slider 2. The occurrence time of the peak velocity slightly increases with γ. The maximum peak velocity of Figure 7 is higher than that of Figure 6. In addition, the predominant period of P wave of an event at slider 2 is shorter in Figure 7 than in Figure 6. This might be due to a shorter U_{c2} (faster friction drop) in the former than a longer U_{c2} (slower friction drop) in the latter. Although a peak velocity appears in the waveform of slider 1, its amplitude is very much smaller than that of slider 2. Hence, unlike Figure 5 there is almost only one event during the whole rupture process in Figure 7. In the right-hand-side panels of Figure 7, U/U_{max} at slider 1 (displayed by a solid line)
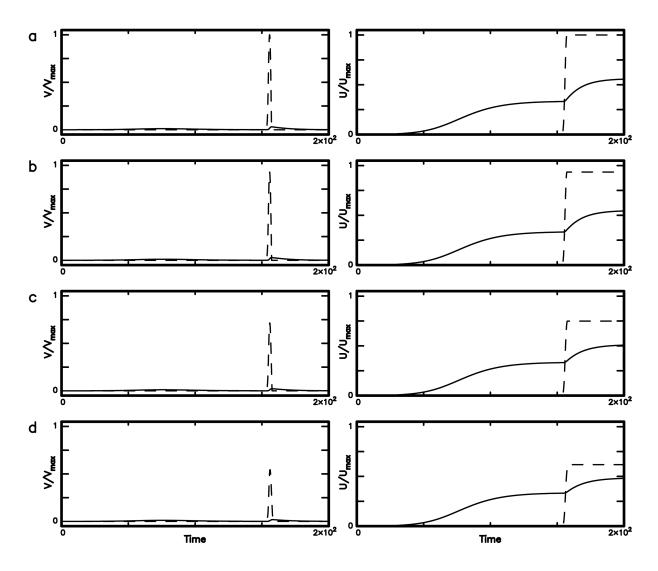

Figure 8. The time sequences of V/V_{max} ($V_{max} = 0.903$) and U/U_{max} ($U_{max} = 1.778$): (a) for $\gamma = 0.00$, (b) for $\gamma = 0.01$, (c) for $\gamma = 0.05$, and (d) for $\gamma = 0.10$ (from weak viscosity ratio to strong viscosity ratio) when $s = 0.17$, $\mu = 1$, $\eta_1 = 10$, $f_{o1} = 1.0$ and $f_{o2} = 1.1$ (with $\phi = 1.1$), and $U_{c1} = 0.5$ and $U_{c2} = 0.1$ (with $\psi = 0.2$).

first appears and increases with time; while that at slider 2 (displayed by a dashed line) suddenly appears for a while after slider 1 moves and then jumps to its peak value in a short time.

Thirdly, it is necessary to consider the effect due to weak seismic coupling (now $s = 0.17$) between the two sliders when $f_{o1} = 1.0$ and $f_{o2} = 1.1$ (with $\phi = 1.1$), and $U_{c1} = 0.5$ and $U_{c2} = 0.1$ (with $\psi = 0.2$), $\eta_1 = 10$, and $\gamma = 0.00, 0.01, 0.05$, and 0.10. Simulation results are displayed in Figure 8. The left-hand-side panels show the NP-PW pattern. After slider 2 stopped, slider 1 still moves and its peak velocity comes after that on slider 2. The peak velocity of slider 1 appears much later than that in Figure 7. This might be due to a fact that it needs a longer time to trigger slider 2 due to weak coupling between the two sliders in Figure 8. Meanwhile, the occurrence time of the peak velocity at slider 2 slightly increases with γ. The maximum peak velocity is higher in Figure 8 than in Figure 7, thus indicating that weaker coupling between two sliders can yield a higher peak velocity than stronger coupling. In addition, the predominant period of P wave of an event at slider 2 is shorter in Figure 8 than in Figure 7. Although a peak velocity appears in the waveform of slider 1, its amplitude is very much smaller than that of slider 2. Unlike Figure 5, there is almost only one event during the whole rupture process in Figure 8. In the right-hand-side panels of Figure 8, U/U_{max} at slider 1 (displayed by a solid line) first appears and increases with time; while U/U_{max} at slider 2 (displayed by a dashed line) suddenly appears for a while after slider 1 moves and then jumps to its peak value in a short time span. In Figures 6-8 the final displacement is higher at slider 2 than at slider 1, but the difference between them decreases with increasing γ.
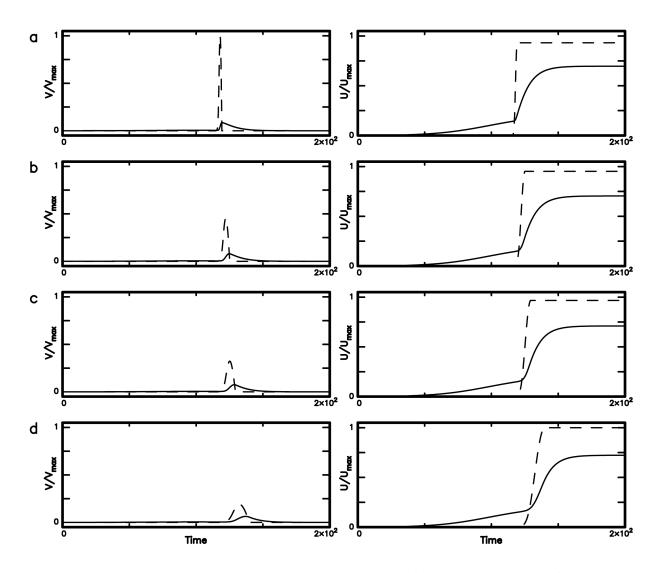

Figure 9. The time sequences of V/V_{max} ($V_{max} = 0.781$) and U/U_{max} ($U_{max} = 1.503$): (a) for $\mu = 1$, (b) for $\mu = 5$, (c) for $\mu = 10$, and (d) for $\mu = 30$ (from weak mass ratio or inertial effect to strong mass ratio or inertial) when $s = 0.48$, $f_{o1} = 1.0$ and $f_{o2} = 1.1$ (with $\phi = 1.1$), $U_{c1} = 0.5$ and $U_{c2} = 0.1$ (with $\psi = 0.2$), and $\eta_1 = 10$ and $\eta_2 = 0$ (with $\gamma = 0$).

4.4 Inertial effect

The inertial effect (represented by $\mu = m_2/m_1$) on the earthquake nucleation is studied for $\mu > 1$. Simulation results are displayed in Figure 9 (with $s = 0.48$) and in Figure 10 (with $s = 0.17$) for $\mu = 1, 5, 10$, and 30 when $f_{o1} = 1.0$ and $f_{o2} = 1.1$ (with $\phi = 1.1$), $U_{c1} = 0.5$ and $U_{c2} = 0.1$ (with $\psi = 0.2$), and $\eta_1 = 10$ and $\eta_2 = 0$ (with $\gamma = 0$). The left-hand-side panels of both Figures 9 and 10 show the NP-PW pattern. The duration time of nucleation phase at slider 1 slightly increases with μ and slightly decreases with increasing peak velocity at slider 2. After slider 2 stopped, slider 1 still moves and its peak velocity comes after that of slider 2. The occurrence times of the peak velocities at both sliders 1 and 2 in Figures 9 and 10 increase with μ and are almost similar to those in Figures 7 and 8, respectively. The occurrence times of the peak velocity in Figure 10 are longer than those in Figure 9. This might be due to a need of a longer time to trigger slider 2 due to smaller s between the two sliders in Figure 10. Meanwhile, the predominant periods of the P wave of an event at sider 2 increases with μ as expected.

The maximum peak velocity is higher in Figure 10 than in Figure 9. This indicates that weaker coupling can yield a higher peak velocity at slider 2 than stronger coupling. The peak velocity is lower at slider 1 than at slider 2 and decreases with μ, especially for small s. Although a peak velocity appears in the waveform of slider 1 in Figures 9 and 10, its amplitude is much smaller than that of slider 2. Unlike Figure 5, there is only one event during the rupture process in Figures 9 and 10.
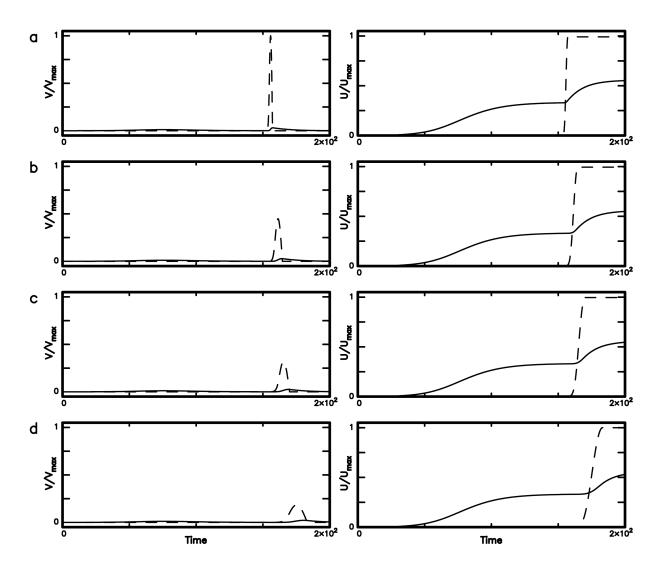

Figure 10. The time sequences of V/V_{max} ($V_{max} = 0.903$) and U/U_{max} ($U_{max} = 1.790$): (a) for $\mu = 1$, (b) for $\mu = 5$, (c) for $\mu = 10$, and (d) for $\mu = 30$ (from weak mass ratio or inertial effect to strong mass ratio or inertial) when $s = 0.17$, $f_{o1} = 1.0$ and $f_{o2} = 1.1$ (with $\phi = 1.1$), $U_{c1} = 0.5$ and $U_{c2} = 0.1$ (with $\psi = 0.2$), and $\eta_1 = 10$ and $\eta_2 = 0$ (with $\gamma = 0$).

In Figures 9 and 10, the peak velocity of P wave of an event at slider 2 decreases with increasing μ. Numerical tests exhibit that the P wave may become a nucleation phase at slider 2 when $\mu > 30$. In the other word, the nucleation phase at slider 1 cannot trigger an event at slider 2 when the mass of the latter is 30 times larger than that of the former. When the densities and fault widths of the two sliders are equal, the fault length of slider 2 is 30 times longer than that of slider 1 when $\mu = 30$. Since the present model is a strike-slip one, the empirical relationship of earthquake magnitude, M, versus fault length, L_f, is: $M = (5.16 \pm 0.13) + (1.12 \pm 0.08)log(L_f)$ [e.g., Wells and Coppersmith, 1994; Wang, 2018]. When $\mu = 30$ or $L_{f2} = 30\,L_{f1}$, the magnitudes are M for slider 1 and $M + 1.65$ for slider 2. Hence, a nucleation phase with a magnitude of M cannot trigger an earthquake with a magnitude of $M + 1.65$.

In the right-hand-side panels of Figures 9 and 10, U/U_{max} at slider 1 first appears and increases with time; while U/U_{max} at slider 2 suddenly appears for a while after slider 1 moves and then jumps to its peak value in a short time span. The difference in final displacement between the two sliders slightly increases with μ and is bigger for small s than for large s. The phenomenon that the final displacement at slider 1 is lower than that at slider 2 might be due to a higher force drop at slider 2 than at slider 1. The duration time of nucleation phase at slider 1 slightly increases with μ. From Figures 9 and 10, the duration time of nucleation phase is shorter for $s = 0.48$ than for $s = 0.17$. This means that seismic coupling can influence the duration time of nucleation phase when $\mu > 1$.

4.5 Combined effects

Simulation results show that the four ratios γ, ϕ, ψ, and μ are important factors in influencing the earthquake nucleation and rupture processes, but the seismic coupling s is a minor one. Except for the cases with equal values on the two sliders for the four ratios, the nucleation phase happens at slider 1 and the P wave appears at slider 2. When $\gamma > 1$, $\phi = 1$, $\psi = 1$, and $\mu = 1$, there is only a very short-duration nucleation phase and the P wave appears very soon after the generation of nucleation phase. This is inconsistent with Figure 1.

Figures 6-10 exhibit the consistence of simulated results with Figure 1. From these figures, the duration time of nucleation phase at slider 1 only slightly increases with μ and final displacement at slider 2. The final displacement at slider 2 represents the size of the large event generated at it. This implicates that the duration time of nucleation phase at slider 1 only weakly depends on the size of an event at slider 2.

When $\psi = 1$ or $\psi < 1$ with $\gamma > 1$, $\phi > 1$, and $\mu = 1$, there is a long-duration nucleation phase at slider 1 and the P wave appears at slider 2 much lately after the generation of nucleation phase. For $\psi = 1$ (see Figures 4 and 5), the simulated waveforms are consistent with Figure 1, but the final displacement of nucleation phase at slider 1 is the same as that of the P wave at slider 2. This indicates equality of energy, which is related to the square of final displacement, at the two sliders. This is questionable, because the energy of nucleation phase is usually lower than that of the mainshock from observations. While, for $\psi < 1$ (see Figures 6-10) the final displacement of nucleation phase is smaller than that of P wave. The difference in the amplitudes between the P wave and nucleation phase decreases with increasing s, increasing γ, or decreasing ψ. The simulated waveforms are consistent with Figure 1. The results are reasonable, because the total energy at slider 1 is less than that at slider 2.

When $\gamma > 1$, $\phi > 1$, and $\psi < 1$, the peak velocity of slider 2 decreases with increasing μ, and becomes very small when $\mu > 30$, even though the final displacement of nucleation phase is still smaller than that of P wave. The degree of similarity of simulated waveforms of these cases (see Figures 9 and 10) with Figure 1 decreases with increasing μ. The upper-bound value of μ to yield transition from nucleation phase to the P wave from observations is 30. Consequently, the optimal conditions for generating the nucleation phase at slider 1 plus the P wave at slider 2 as displayed in Figure 1 are $\gamma > 1$, $\phi > 1$, $\psi < 1$, and $\mu < 30$. Of course, there are upper-bound values for γ and ϕ and a lower-bound value for ψ as mentioned in the last sections. Note that the upper-bound value of a certain ratio depends on the values of other ratios.

4.6 Comparisons with other studies

From observations, Ellsworth and Beroza [1995] and Beroza and Ellsworth [1996] claimed that the duration time of nucleation phase is positively related to the earthquake magnitude. While Mori and Kanamori [1996] observed that in a large magnitude range, the P waves of the event behind the nucleation phase are independent on the shape of nucleation phase. Figures 6-10 clearly exhibit independence of P wave of an event at slider 2 on the shape

of nucleation phase at slider 1. The present simulation results are consistent with the observations by Mori and Kanamori [1996].

Numerous authors studied the frictional effect on nucleation phases. Tal et al. [2018] numerically studied the effect of fault roughness with amplitude of b_r on the nucleation process in the presence of a rate- and state-dependent friction law. The roughness can yields local barriers and makes the nucleation process complicated. They also found an increase in nucleation length with b_r. Considering a broad weak zone with a locally strong asperity on a fault plane, Shibazaki and Matsu'ura [1995] found that in the dynamic rupture of the asperity, there are aseismic slip and foreshock or pre-event, depending on the peak stress of the asperity, preceding the main rupture and the rupture of the asperity accelerates the nucleation of main rupture. This study indicates the influence of heterogeneous friction strengths on the generation of nucleation phase. Schmitt et al. [2015] addressed the importance of time-dependent stress heterogeneity on nucleation. The present results for different values of ϕ at the two sliders as shown in Figures 5-7 may meet those obtained by the three groups of researchers.

Using an infinite elastic model with slip-dependent friction, Ionescu and Campillo [1999] found the influence of the shape of the friction law and fault finiteness on the duration of nucleation phase and the duration varies when the fault length has the order of the characteristic length of the friction law. Figure 7 is consistent with theirs.

Based on an infinite elastic model with slip-dependent friction, Shibazaki and Matsu'ura [1992] assumed that the transition process includes three phases: phase-I for the low quasi-static nucleation, phase-II for the onset of dynamic ruptured with slow rupture growth in the absence of seismic-wave radiation, and phase-III for the high-speed rupture propagation with seismic-wave radiation. Shibazaki and Matsu'ura [1993] further found that the accelerating stage from phase-II to phase-III is related to the presence of nucleation phase in the front of the main P wave. Their results are similar to those obtained by Ueda et al. [2014, 2015] and Kawamura et al. [2018]. The results of this study and Wang [2017a] only show two stages which are comparable with the phase-I and phase-III stages proposed by Shibazaki and Matsu'ura [1992, 1993]. From the analytic solutions of an infinite elastic model with a slip-dependent friction, Campillo and Ionescu [1997] expressed how the initiation phase determines the transition to the P wave and claimed that the transition is controlled by an apparent supersonic velocity of the rupture front. However, the present result does not meet their conclusion. According to an infinite elastic model with rate- and state-dependent friction, Segall and Rice [2006] divided the weakening processes of ruptures into the nucleation regime dominated by rate and state frictional weakening and a transition regime to thermal pressurization. In the present study, the thermal-pressurized slip-weakening friction is considered during the whole rupture process and the results show a transition from the nucleation phase with smaller f_{o1} and smaller U_{c1} at slider 1 to the P wave with larger f_{o2} and larger U_{c2} at slider 2. Hence, the present result could be only partly consistent with theirs.

However, the main difference between the present study and previous ones is that the nucleation phase appears at slider 1 does not disappear after the presence of P wave at slier 2. This might be due to a use of two fault segments (i.e., a two-body model) in this study and a use of one fault segment (i.e., a one-body or 1-D model) by others. Like Wang [2017a], both friction and viscosity are considered as important factors in yielding the transition from quasi-static motions to dynamic ruptures in this study; while only friction was proposed in others.

5. Conclusions

We study the frictional and viscous effects on earthquake nucleation based on a two-body spring-slider model in the presence of thermal-pressurized slip-dependent friction and viscosity. The seismic coupling of the system is represented by the ratio of coil spring K between two sliders and the leaf spring L between a slider and the background plate and denoted by $s = K/L$. The s is not a significant factor in generating the nucleation phase. The masses of the two sliders are m_1 and m_2, respectively. The frictional and viscous effects at slider i (i = 1, 2) are specified by the static friction force, f_{oi}, the characteristic displacement, U_{ci}, and viscosity coefficient, η_i, respectively. Simulation results show that friction and viscosity can both lengthen the natural period of the system and viscosity increases the duration time of motion of the slider. Higher viscosity causes lower particle velocities than lower viscosity. The ratios $\gamma = \eta_2/\eta_1$, $\phi = f_{o2}/f_{o1}$, $\psi = U_{c2}/U_{c1}$, and $\mu = m_2/m_1$ are four important factors in influencing the generation of nucleation phases. When $\gamma > 1$, $\phi = 1$, $\psi = 1$, and $\mu = 1$, the nucleation phase is generated at slider 1 and the P wave appear at slider 2. But, the P wave appears very soon after the generation of nucleation phase. When $\gamma > 1$, $\phi > 1$, $\psi \geq 1$, and $\mu = 1$, the P wave appears much lately after the generation of nucleation phase. When $\psi \geq 1$, the final displacement of nucleation phase is almost equal to that of P wave. When $\psi < 1$, the final displacement of nucleation

phase is smaller than that of P wave. The difference in the amplitudes between the P wave and nucleation phase decreases when either s or γ increases and ψ decreases. The peak velocity of P wave of an event at slider 2 decays with increasing μ, thus suggesting that the inertial effect is important on the rupture processes. Consequently, when $s > 0.17, \gamma > 1, 1.15 > \phi > 1, \psi < 1$, and $\mu < 30$ simulation results exhibit the generation of nucleation phase at slider 1 and the formation of P wave of an event at slider 2. The results are consistent with the observations and suggest the possibility of generation of nucleation phase on a sub-fault. This answer the question addressed in this study.

Figures 6-10 exhibit independence of P wave on the shape of nucleation phase. In addition, the duration time of nucleation phase at slider 1 only slightly increases with μ and the size of an event at slider 2.

References

Andrews, D.J. (1976). Rupture velocity of plane strain shear cracks, J. Geophys. Res., 81, 5679-5687.

Beeler, N.M. (2004). Review of the physical basis of laboratory-derived relations for brittle failure and their implications for earthquake occurrence and earthquake nucleation, Pure Appl. Geophys., 161, 1853-1876, DOI:10.1007/s00024-004-2536-z.

Beroza, G.C. and W.L. Ellsworth (1996). Properties of the seismic nucleation phase, Tectonophys., 261, 209-227.

Bizzarri, A. (2009). What does control earthquake ruptures and dynamic faulting? A review of different competing mechanism, Pure Appl. Geophys., 166, 741-776.

Bizzarri, A. (2011a). Dynamic seismic ruptures on melting fault zones, J. Geophys. Res., 116, B02310, doi:10.1029/2010JB007724.

Bizzarri, A. (2011b). Temperature variations of constitutive parameters can significantly affect the fault dynamics, Earth Planet. Sci. Lett., 306, 72-278, doi:10.1016/j.epsl.2011.04.009.

Brantut N., J. Sulem, and A. Schubnel (2011). Effect of dehydration reactions on earthquake nucleation: Stable sliding, slow transients, and unstable slip, J. Geophys. Res., 116, B05304, doi:10.1029/2010JB007876.

Brune, J. (1979). Implications of earthquake triggering and rupture propagation for earthquake prediction based on premonitory phenomena, J. Geophys. Res., 84, 2195-2198.

Burridge, R. and L. Knopoff (1967). Model and theoretical seismicity, Bull. Seism. Soc. Am., 57, 341-371.

Campillo, M. and I.R. Ionescu (1997). Initiation of antiplane shear instability under slip dependent friction, J. Geophys. Res., 102, 20263-20371.

Carlson, J.M., J.S. Langer, B.E. Shaw, and C. Tang (1991). Intrinsic properties of a Burridge-Knopoff model of an earthquake fault, Phys. Rev. A, 44, 884-897.

Das, S. and C.H. Scholz (1981). Theory of time-dependent rupture in the Earth, J. Geophys. Res., 86, B7, 6039-6057.

Dieterich, J.H. (1979). Modeling of rock friction 1. Experimental results and constitutive equations, J. Geophys. Res., 84, 2161-2168.

Dieterich, J.H. (1981). Potential for geophysical experiments in large scale tests, Geophys. Res. Lett., 8, 653-656.

Dieterich, J.H. (1986). A model for the nucleation of earthquake slip. In: Earthquake Source Mechanics, Das et al. (eds.), Geophysical Monograph 37, Maurice Ewing AGU, 6, 37-47.

Dieterich, J.H. (1992). Earthquake nucleation on faults with rate- and state-dependent strength, Tectonophys., 211, 115-134.

Dragoni M. and E. Lorenzano (2015). Stress states and moment rates of a two-asperity fault in the presence of viscoelastic relaxation, Nonlin. Processes Geophys., 22, 349-359.

Dragoni M., and E. Lorenzano (2017). Dynamics of a fault model with two mechanically different regions, Earth Planets Space, 69, 145-159.

Dragoni M. and A. Piombo (2015). Effect of stress perturbations on the dynamics of a complex fault, Pure Appl. Geophys., 172, 2571-2583.

Dragoni M. and S. Santini (2015). A two-asperity fault model with wave radiation, Phys. Earth Planet. Inter., 248, 83-93.

Dragoni M. and S. Santini (2017). Effects of fault heterogeneity on seismic energy and spectrum, Phys. Earth Planet. Inter., 273, 11-22.

Dragoni M. and A. Tallarico (2016). Complex events in a fault model with interacting asperities, Phys. Earth Planet. Inter., 257, 115-127.

Ellsworth, W.L. and G.C. Beroza (1995). Seismic evidence for an earthquake nucleation phase, Science, 268, 851-855.

Ellsworth, W.L. and G.C. Beroza (1998). Observation of the seismic nucleation phase in the Ridgecrest, California, earthquake sequence, Geophys. Res. Lett., 25(3), 401-404.

Galvanetto, U. (2002). Some remarks on the two-block symmetric Burridge-Knopoff model, Phys. Letts. A., 293, 251-259.

Iio, Y. (1992). Slow initial phase of the P-wave velocity pulse generated by microearthquakes, Geophys. Res. Lett., 19, 477-480.

Iio, Y. (1995). Observation of the slow initial phase of microearthquakes: Implications for earthquake nucleation and propagation, J. Geophys. Res., 100, 15333-15349

Ionescu, I.R. and M. Campillo (1999). Influence of the shape of the friction law and fault finiteness on the duration of initiation, J. Geophys. Res., 104(B2), 3013-3024.

Kato N, K. Yamamoto, and T. Hirasawa (1994). Microfracture processes in the breakdown zone during dynamic shear rupture inferred from laboratory observation of near-fault high frequency strong motion, Pure Appl. Geophys., 142, 713-734.

Kawamura H., M., Yamamoto, and Y. Ueda (2018). Slow-slip phenomena represented by the one-dimensional Burridge-Knopoff model of earthquakes, J. Phys. Soc. Japan, 87, 053001, https://doi.org/10.7566/JPSJ.87.053001.

Kittel, C., W.D. Knight, and M.A. Ruderman (1968). Mechanics. Berkeley Physics Course, Vol. 1, McGraw-Hill Book Co., New York, N.Y., 480.

Lachenbruch, H. (1980). Frictional heating, fluid pressure and the resistance to fault motion, J. Geophys. Res., 85, B11, 6097-6112.

Latour,S., A. Schubnel, S. Nielsen, R. Madariaga, and S.Vinciguerra (2013). Characterization of nucleation during laboratory earthquakes, Geophys. Res. Lett., 40, 5064-5069, doi:10.1002/grl.50974.

Lee, T C. and P.T. Delaney (1987), Frictional heating and pore pressure rise due to a fault slip, Geophys. J. R. Astron. Soc., 88, 3, 569-591.

Lorenzano E. and M. Dragoni (2018). Complex interplay between stress perturbations and viscoelastic relaxation in a two-asperity fault model, Nonlin. Processes Geophys., 25, 251-265.

Lu X, A.J. Rosakis, and N. Lapusta (2010). Rupture modes in laboratory earthquakes: Effect of fault prestress and nucleation conditions, J. Geophys. Res., 115, B12302, doi:10.1029/2009JB006833.

Mase, C.W. and L. Smith (1987). Effects of frictional heating on the thermal, hydrologic, and mechanical response of a fault, J. Geophys. Res., 92, 6249-6272.

Mori, J. and H. Kanamori (1996). Initial rupture of earthquakes in the 1995 Ridgecrest, California sequence, Geophys. Res. Lett., 2, 2437-2440.

Ohnaka, M. (1992). Earthquake source nucleation: a physical model for short-term precursors, Tectonophys. 211, 149-178.

Ohnaka, M. and Y. Kuwahara (1990). Characteristic features of local breakdown near a crack-tip in the transition zone from nucleation to dynamic rupture during stick-slip shear failure, Tectonophys., 175, 197-220.

Ohnaka, M. and T. Yamashita (1989). A cohesive zone model for dynamic shear faulting based on experimentally inferred constitutive relation and strong motion source parameters, J. Geophys. Res., 94, 4089-4104

Ohnaka, M., Y. Kuwahara, and K. Yamamoto (1987). Constitutive relations between dynamic physical parameters near a tip of the propagating slip zone during stick-slip shear failure, Tectonophys., 144,109-125

Press, W.H., B.P. Flannery, S.A. Teukolsky, and W.T. Vetterling (1986). Numerical Recipes. Cambridge Univ. Press, Cambridge, 818.

Rice J. R. (1993). Spatio-temporal complexity of slip on a fault, J. Geophys. Res., 98, 9885-9907.

Rice, J.R. (2006). Heating and weakening of faults during earthquake slip, J. Geophys. Res., 111, B05311, doi:10.1029/2005JB004006.

Rice, J.R., N. Lapusta, and K. Ranjith. (2001). Rate and state dependent friction and the stability of sliding between elastically deformable solids, J. Mech. Phys. Solids, 49, 1865-1898.

Roy, M. and C. Marone (1996). Earthquake nucleation on model faults with rate- and state-dependent friction: Effects of inertia, J. Geophys. Res., 101(B6), 13919-13932.

Jeen-Hwa Wang

Ruff, L.J. (1992). Asperity distributions and large earthquake occurrence in subduction zones, Tectonophys., 211, 61-83.

Ruiz, S., F. Aden-Antoniow, J.C. Baez, C. Otarola, B. Potin, F. del Campo, P. Poli, C. Flores, C. Satriano, F. Leyton, R. Madariaga, and P. Bernard (2017). Nucleation phase and dynamic inversion of the Mw6.9 Valparaíso 2017 earthquake in Central Chile, Geophys. Res. Lett., 44, 10290-10297, doi.org/10.1002/2017GL075675.

Scholz, C.H., P. Molnar, and T. Johnson (1972). Detailed studies of frictional sliding of granite and implications for the earthquake mechanism, J. Geophys. Res., 77, 6392-6406.

Schmitt, S.V., P. Segall, and E.M. Dunham (2015). Nucleation and dynamic rupture on weakly stressed faults sustained by thermal pressurization, J. Geophys. Res. Solid Earth, 120, 7606-7640 doi:10.1002/2015JB012322.

Segall, P. and J.R. Rice (2006). Does shear heating of pore fluid contribute to earthquake nucleation?. J. Geophys. Res., 111, B09316, doi:10.1029/ 2005JB004129

Shibazaki, B. and M. Matsu'ura (1992). Spontaneous processes for nucleation, dynamic propagation, and stop of earthquake rupture. Geophys. Res. Lett., 19, 1189-1192.

Shibazaki, B. and M. Matsu'ura (1993). Transition process from nucleation to high-speed rupture propagation: Scaling from stick-slip experiments to natural earthquakes (abstract), Eos Trans. AGU, 47, 410.

Shibazaki, B. and M. Matsu'ura (1995). Foreshocks and pre-events associated with the nucleation of large earthquakes, Geophys. Res. Lett., 22(10), 1305-1308.

Tal, Y., B.H. Hager, and J.P. Ampuero (2018). The effects of fault roughness on the earthquake nucleation process, J. Geophys. Res., 123, 437-456, doi.org/10.1002/ 2017JB014746.

Turcotte, D.L. (1992). Fractals and Chaos in Geology and Geophysics, Cambridge Univ. Press, Cambridge, 221.

Ueda Y., S. Morimoto, S. Kakui, T. Yamamoto, and H. Kawamura (2014). Nucleation process in the Burridge-Knopoff model of earthquakes, Europhys. Lett., 106 69001, doi:10.1209/0295-5075/106/69001.

Ueda Y., S. Morimoto, S. Kakui, T. Yamamoto, and H. Kawamura (2015). Dynamics of nucleation process represented by the Burridge-Knopoff mode, Eur. Phys. J. B, 88, 235, DOI:10.1140/epjb/e2015-60499-0.

Umeda, Y. (1990). High-amplitude seismic waves radiated from the bright spot of an earthquake, Tectonophys., 135, 81-92.

Wang, J.H. (1995). Effect of seismic coupling on the scaling of seismicity, Geophys. J. Int., 121, 475-488.

Wang, J.H. (2007). A dynamic study of the frictional and viscous effects on earthquake rupture: a case study of the 1999 Chi-Chi earthquake, Taiwan, Bull. Seism. Soc. Am., 97(4), 123-1244.

Wang, J.H. (2013). Stability analysis of slip of a one-body spring-slider model in the presence of thermal pressurization, Ann. Geophys., 56(3), R03332, doi:10.4401/ ag-5548.

Wang, J.H. (2016). Slip of a one-body spring-slider model in the presence of slip-weakening friction and viscosity, Ann. Geophys., 59, 5, S0541, doi:10.4401/ag-7063

Wang, J.H. (2017a). Frictional and viscous effects on the nucleation phase of an earthquake nucleation, J. Seismol., 21(6), 1517-1539.

Wang, J.H. (2017b). Slip of a two-degree-of-freedom spring-slider model in the presence of slip-weakening friction and viscosity, Ann. Geophys., 60, 6, S0659, doi:10.4401/ag-7295.

Wang, J.H. (2018). A review on scaling of earthquake faults, Terr. Atmos. Ocean. Sci., 29(6), 589-610.

Wang, J.H. (2020). Inertial effect on interaction between two earthquake faults, Ann. Geophys., 63, 2, SE221. doi:10.4401/ag-8136

Wells, D.L. and K.J. Coppersmith (1994). New empirical relationships among magnitude, rupture length, rupture width, rupture area, and surface displacement, Bull. Seism. Soc. Am., 84, 974-1002.

CORRESPONDING AUTHOR: Jeen-Hwa WANG,
Institute of Earth Sciences, Academia Sinica, Taipei, Taiwan
and Department of Earth Sciences, National Central University, Taoyuan, Taiwan
e-mail: jhwang@earth.sinica.edu.tw